A Current-fed Three-port DC/DC Converter for Integration of On-board Charger and Auxiliary Power Module in Electric Vehicles

Liyan Zhu
Department of Electrical Engineering and Computer Science
University of Tennessee
Knoxville, TN, USA
liyan@utk.edu

Hua Bai
Department of Electrical Engineering and Computer Science
University of Tennessee
Knoxville, TN, USA
hbai2@utk.edu

Alan Brown
HELLA Electronics Corporation
Northville Township, MI
alan.brown@hella.com

Lukas Keuck
HELLA GmbH & Co. KGaA
Lippstadt / Germany
Lukas.Keuck@hella.com

Abstract: **On-board charger (OBC) and auxiliary power module (APM) are two major power electronic units in electric vehicles (EVs). OBC is the interface between the grid and HV propulsion battery, and the APM is the bridge connecting the HV system and LV system inside the EV. To save the cost and shirk the size, this paper proposed a three-port current-fed triple-active bridge (CFTAB) converter to integrate OBC with APM both electrically and magnetically. Compared with state-of-art integration approaches, the proposed converter features a simple structure, free of function-select switches, and fewer transformer turns. With the corresponding power decoupling method developed, the proposed topology also allows charging HV battery and LV battery simultaneously. Due to the current-fed nature, there is no need for large output capacitors, and much lower current stress is exhibited. In addition, an integrated prototype for 11kW/250V~450V OBC plus 3.5kW/10V~16V APM is developed to prove the superiorities of the proposed integrated charger.**

Index Terms**: Auxiliary power module; On-board charger; Integrated charger; Electric vehicles; Three-port converters.**

I. INTRODUCTION

Power electronics units alter the form of energies and connect multiple power sources and loads in electric vehicles (EVs). For example, the on-board charger (OBC) accepts the AC input and converts it to DC to charge the propulsion battery. An Auxiliary Power Module (APM) steps down the HV DC bus voltage to the LV bus to power non-propulsion loads and charges the LV battery[1]. Usually, the OBC and the APM are separated units in EVs. They are designed at different power levels, e.g., 11kW or 22kW for OBC and 2.5kW or 3.5kW for the APM. Even though the APM has lower power rating, due to the low output voltage of APM, it has much higher current stress. For example, delivering 3.5kW @12V means an RMS current of 290A. To handle such a high current, the transformer winding has to be designed with a thick gauge, and more devices need to be paralleled for heat dissipation.

The seperate OBC and APM present a large volume and high cost. However, they usually share some similar and commonly used topologies. As shown in Fig. 1, the OBC and APM both have the primary side bridges, transformers, and DC-link capacitors. To save the cost and shrink the size, it is of importance to integrate two units using a three-winding transformer, as illustrated in Fig. 2.

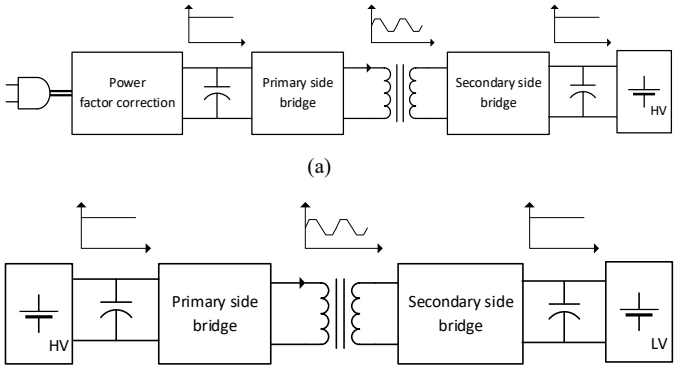

Fig. 1 Commonly used structures for (a) OBC and (b) APM

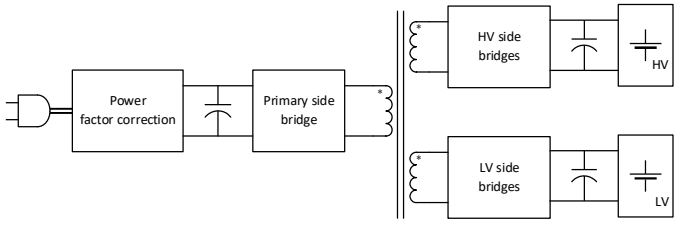

Fig. 2 Concept of electric-magnetically integrated charger

However, state-of-art integrating approaches present limitations. Some realize the integration electrically. For example, [2][3] proposed to use additional selection switches to reconfigure the topology to select which battery to charge. Another solution is adopting a dual transformer based converter to facilitate power decoupling[4]. However, these methods still need multiple transformers. Meanwhile, additional function-select switches are needed. Others integrate the OBC and APM at the transformer stage. Usually, a three-winding transformer

is adopted to share the core between OBC and APM. This type of charger has a higher integration level, but encounter some issues, such as power decoupling and challenging transformer design. For example, a resonant converter based integrated charger encounters the challenge of coupled output power. Because of lack of control freedom, the power flows to HV port and LV port without regulation, which is unacceptable for the EV charging. To solve the problem, [5]–[8] proposed to use an extra stage in series with the resonant converter to regulate the output power, which lowers the efficiency and power density.

Voltage-fed triple-active bridge (VFTAB) based integrated chargers are reported in [9][10]. However, these converters present high current stress on all three ports, yielding low efficiency. In addition, determined by the DC link voltage and the LV battery voltage, the transformer turn ratio is high.

Some other topologies, such as [11][12] proposed to use a three-winding transformer along with function-select switches for different charging modes. The power flow can be decoupled. The common issue is the need for additional selection switches and can not charge HV and LV batteries at the same time.

To mitigate all the shortcomings mentioned above, this paper proposed a novel current-fed three-ports converter, as shown in Fig. 3. The converter has three ports: the primary side, HV side and LV side, which are connected to PFC output, HV battery and LV battery, respectively. The Ls1~Ls3 are the leakage inductance of the transformer. Lo1 and Lo2 are negatively coupled inductors for the HV output filter. Similarly, Lo3 and Lo4 are coupled inductors for the LV output. C_{hv} and C_{lv} are clamping capacitors and used to maintain a high DC voltage to reduce current stress at both transformer secondary sides. The power flow between ports is controlled by the phase shift between them. Compared with aforementioned topologies, the proposed one has multiple advantages. Firstly, the current-fed port boosts the LV side voltage to a higher value, which reduces the turn ratio and facilitates the transformer design. Secondly, the duty cycles are additional control freedoms, enabling the possibility of full-power-range zero-voltage-switching (ZVS). The major portion of the current of low-side switches at HV and LV ports is negative, representing much lower current stress than voltage-fed converters.

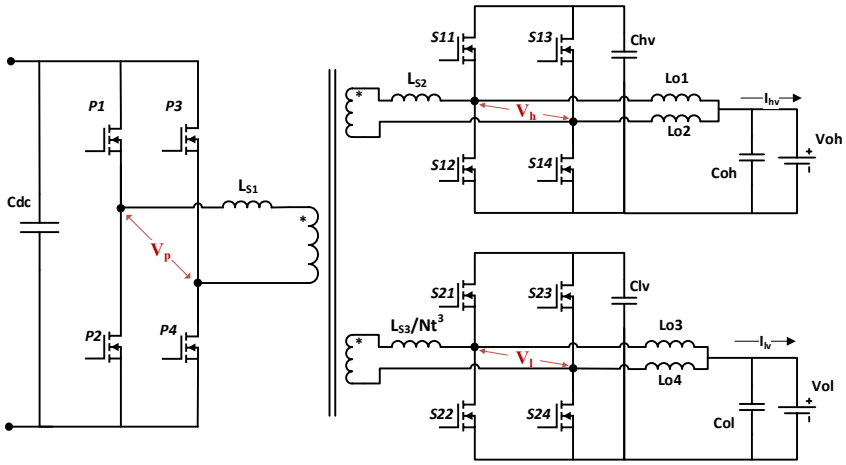

Fig. 3 The topology of the proposed converter for the integrated charger

II. CFTAB Based Charger Design

Five control variables are involved in the operation of CFTAB, i.e., the $D_p, D_h, D_l, Ps_h,$ and Ps_l. The first three variables D_p~D_l are duty cycles of high side switches at the primary side, HV side and LV side, respectively. Ps_h and Ps_l are the phase shifts for the HV side and LV side, referred to the primary side, as illustrated in Fig. 4. Note that the PWMs are center-aligned, which means when Ps_h or Ps_l equals zero. The corresponding transformer terminal voltage V_h or V_l are also center aligned with primary side voltage V_p, yielding zero power between two ports. For each port, the first phase leg (P1, S11, S21) and second one (P2, S12, S22) always have a 180° phase difference, which guarantees V_P, V_h *and* V_l are always symmetric around zero to avoid the accumulation of DC bias in the transformer. The duty cycle is defined as turn-on time over the switching period T_s, and phase shift is delay time over $\frac{T_s}{2}$. normal values of all the control variables are 0~0.5, when the power flows from the primary side to HV or LV sides.

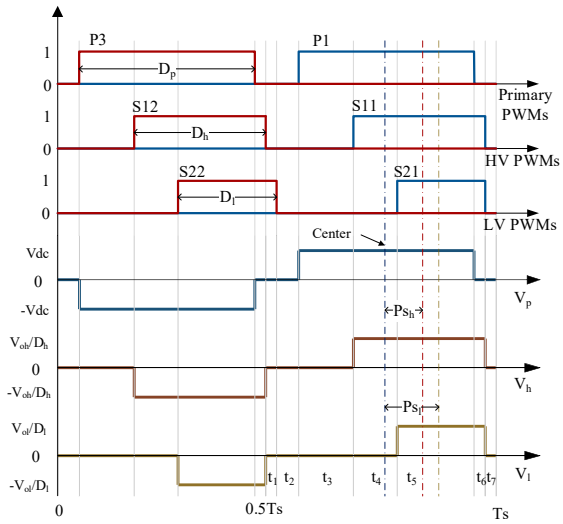

Fig. 4 PWMs timing and control variables

a. CFTAB Modeling

CFTAB has a similar structure as VFTAB, of which its operation principle, power flow and ZVS range are well studied in previous literature [13]–[15]. Its complexity lies in that HV and LV side transformer terminal voltages are not only related to the battery voltages but also involves with duty cycles of D_h and D_l. The peak clamping voltage at the HV side is V_{oh}/D_h, while that at the LV side is V_{ol}/D_l. In addition, duty cycles also affect the timing sequence of terminal voltages, yielding hundreds of operation modes. It is not feasible to calculate power and ZVS current for all operation modes manually. Thus a generalized CFTAB model will be derived in this paper.To facilitate the calculation, the transformer in the Fig. 3 will be transformed to Δ model, as shown in Fig. 5.

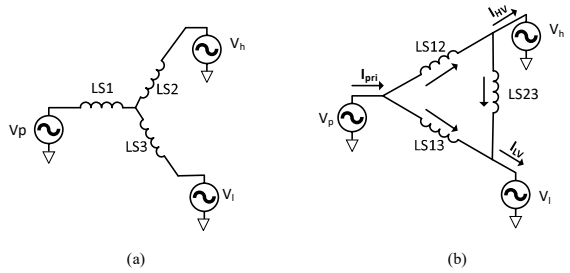

Fig. 5 Transformer model (a) Wye model, (b) Δ model

$$\begin{cases} Ls_{12} = \dfrac{Ls_1Ls_2 + Ls_1Ls_3 + Ls_2Ls_3}{Ls_3} \\ Ls_{13} = \dfrac{Ls_1Ls_2 + Ls_1Ls_3 + Ls_2Ls_3}{Ls_2} \\ Ls_{23} = \dfrac{Ls_1Ls_2 + Ls_1Ls_3 + Ls_2Ls_3}{Ls_1} \end{cases} \tag{1}$$

The leakage inductance in the Δ model can be obtained by (1), and the peak voltage of V_h, V_l is

$$\begin{cases} Peak(V_h) = \dfrac{V_{oh}}{D_h} \\ Peak(V_l) = \dfrac{V_{ol}}{D_l} \times N_t \end{cases} \tag{2}$$

Where N_t is the transformer turn ratio of primary side winding over LV side winding. With the voltage and inductance in Fig. 5 available, we can easily calculate the current increment ΔI in each time interval (t_1~t_7 in Fig. 4) for all three ports using (3), where the subscript n is the index of time intervals.

$$\begin{cases} \Delta I_{pn} = \Delta I_{Ls12} + \Delta I_{Ls13} = \left(\frac{V_{pn}-V_{hn}}{L_{s12}} + \frac{V_{pn}-V_{ln}}{L_{s13}}\right) \times t_n \\ \Delta I_{hn} = \Delta I_{Ls12} - \Delta I_{Ls23} = \left(\frac{V_{pn}-V_{hn}}{L_{s12}} - \frac{V_{hn}-V_{ln}}{L_{s23}}\right) \times t_n \\ \Delta I_{ln} = \Delta I_{Ls13} + \Delta I_{Ls23} = \left(\frac{V_{pn}-V_{ln}}{L_{s13}} + \frac{V_{hn}-V_{ln}}{L_{s23}}\right) \times t_n \end{cases} \tag{3}$$

Note (3) is only used to calculate the current increment in each time interval. To calculate the initial current of every half peroid, the summation of current increment in all time intervals is needed. The summation equals twice the initial current, but with opposite polarity in the steady state, as shown in (4). With (3) and (4), the initial transformer current can be easily solved then the current for all time intervals.

$$\begin{cases} \sum_{n=1}^{7} \Delta I_{pn} = -2I_{p1} \\ \sum_{n=1}^{7} \Delta I_{hn} = -2I_{h1} \\ \sum_{n=1}^{7} \Delta I_{ln} = -2I_{l1} \end{cases} \tag{4}$$

However, for the current-fed port the transformer current is not enough to calculate the device switching-on and switching-off current. Using first phase leg of the LV side shown in Fig. 6 as an example. Here $I_{zvs} = I_L - I_{Lo}$. To calculate the accurate ZVS current for the high-side switch, the coupled inductors' current also needs to be considered. The coupled inductors have been well studied in previous literature[16], [17]. The current ripple can be solved by (21) in [18]. To avoid repeating, the equation will be skipped in this paper.

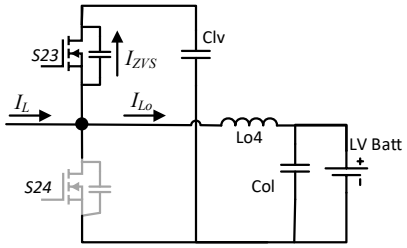

Fig. 6 ZVS current determined by the transformer and coupled inductors

b. Design considerations and operation modes

Multiple key parameters need to be determined when applying the CFTAB to an integrated charger, such as the DC link voltage, transformer turn ratio, clamp capacitor voltages, etc. The specifications of the charger are summarized in the Table. I.

TABLE. 1 INTEGRATED CHARGER SPECIFICATIONS

Input voltage	1P 240V/ 3P 480V
HV battery voltage	250V~450V
LV battery voltage	10~16V
Max output power for HV port	11kW
Max output power for LV port	3.5kW

To incorporate the 3P/480V grid voltage, the DC link voltage has to be higher than the peak of line-to-line voltage. Thus a 750V DC bus voltage is selected as rated. Then, the turn ratio of the transformer is design at 12:12:1 for the primary side, HV side, and LV side. The nominal transformer terminal voltages for HV and LV are calculated as 750V and 60V. 1.2kV SiC MOSFETs for primary and HV sides and 100V Si MOSFETs for LV side are adopted.

Voltage match control is usually adopted for a current-fed converter to minimize transformer current[19], [20]. The control method is easy but suffers from high circulating current and losing of ZVS at light load. Instead, this paper targets full range ZVS and minimizes reactive power. Voltage mismatch

control with extended duty cycle is then developed. Here the duty cycle is no longer used to boost the battery voltage to match the transformer winding voltage induced from the primary side. Instead, it is used to secure ZVS and minimize reactive power. In addition, an extended duty cycle for the HV port is adopted. Usually, for the current-fed converter, the duty cycle is operating lower than 0.5 for the sake of ZVS, which however is not suited for the integrated charger. For example, when the HV battery is fully charged at 450V, even $D_h = 0.5$ yields a clamping voltage on C_{hv} up to 900V. Thus, this paper extends the D_h to be higher than 0.5 when the battery voltage is high. At the same time, the ZVS can still be secured by compensation from the primary side.

With the model for transformer current and coupled inductor current ready, an adaptive optimization method was developed to select the proper operation modes for extended voltage mismatch control. The selected operation modes are classified by the battery voltage instead of the power level. The reason is full power range ZVS is already set as the top priority in the optimization process. Duty cycles are then further optimized only based on battery voltage for reduced reactive power. With optimized values, the typical transformer waveforms are plotted in Fig. 7. ZVS currents for all three ports are plotted in Fig. 8 using the color bar. It's clear for a given battery voltage, optimized duty cycles can always secure ZVS at any output power. More detailed operation modes can be generated other than shown in Fig. 7 to smooth the transition. Limited by length, they are not illustrated in this paper.

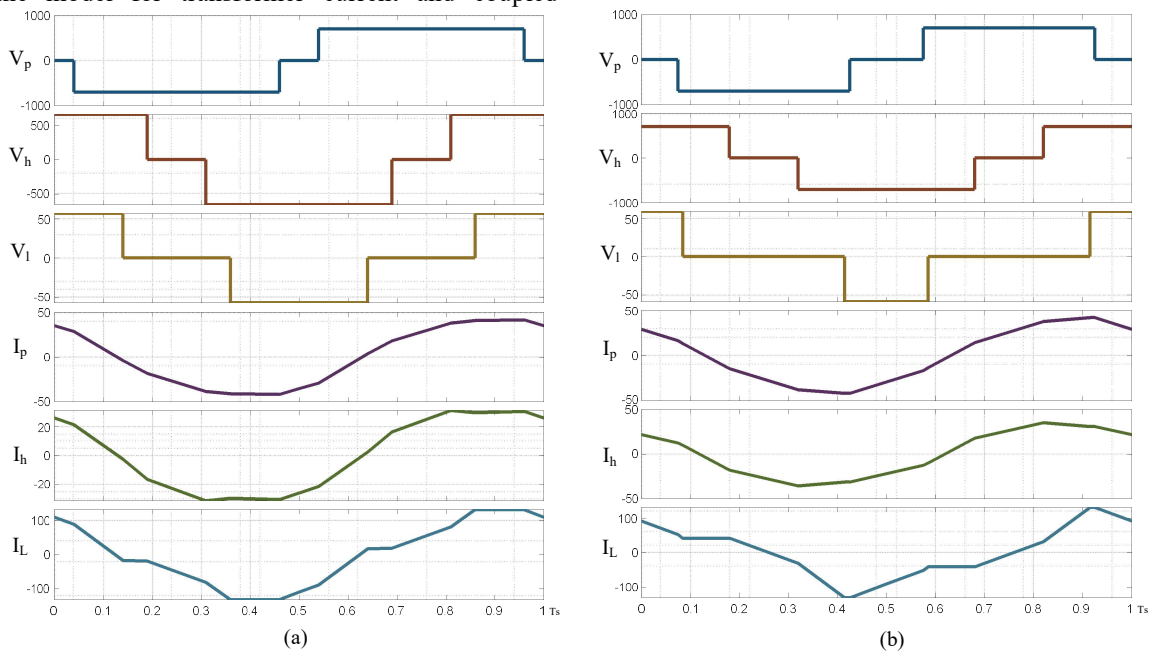

Fig. 7 Transformer waveform with optimized duty cycles (a) 11kW@250V for HV and 3kW@16V for LV (b) 11kW@450V for HV and 3kW@10V for LV

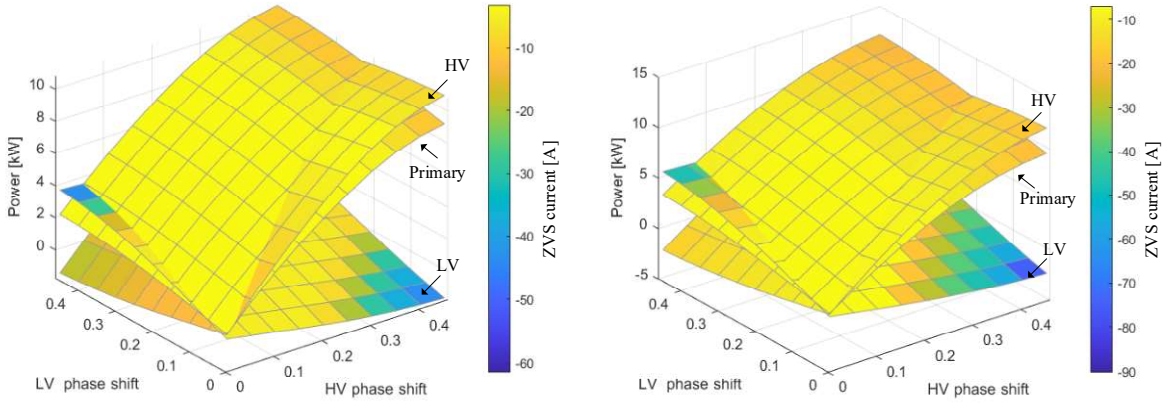

Fig. 8 Full range ZVS with optimized duty cycles (a) 250V for HV and 16V for LV (b) 450V for HV and 10V for LV

Current-fed converters usually don't need bulky output capacitors. Instead, the output inductors are necessary. Negatively coupled inductors are adopted in this paper to shrink the output filter size. Thank for the interleaving operation of the phase legs, the coupled inductor cancels the DC output current, and only AC ripples are the source of magnetic fluxes. In this case, the core size of the inductors can be significantly reduced. In addition, due to interleaving, the output current ripple is also significantly suppressed.

III. PROTOTYPE AND EXPERIMENTS

Based on the analysis and design above, a prototype is built to verify the design, as shown in Fig. 9. Both the PFC stage and CFTAB stage are included. The key parameters of the charger are listed in the Table. II.

TABLE. 1 INTEGRATED CHARGER PARAMETERS

Transformer turn ratio	12:12:1
XFMR primary side leakage inductances	12uH
XFMR HV side leakage inductances	12uH
XFMR LV side leakage inductances	0.24uH
XFMR Magnetizing inductances	260uH
Rated DC link voltage	750V
HV clamp capacitor voltage	~750V
LV clamp capacitor voltage	~60V
Primary/HV side switches	C3M0032120K
LV side switches	IRF100P219

The charger is tested to full power with a 750V DC Bus voltage, 11kW power delivered at 350V for HV port, and 3.5kW power delivered at 12V for LV port separately. The key waveforms of the transformer are shown in Fig. 13 and Fig. 11.

Fig.13~14 show the current stress for current-fed ports. Comparing Fig. 13 to Fig. 14, current-fed ports show different current stress on high-side and low-side switches. For high-side switches, the current is used to charge and discharge the clamp capacitor. Thus it's a circulating current without flowing to load. For low-side switches, Ids is mainly the load current and almost always negative, securing ZVS with low switching-off current, a critical benefit for the LV port. Compared with conventional voltage-fed converters, the proposed converter does not suffer from high current stress on both-side switches.

The proposed design also shows high power density. As shown in Fig. 9. modular design is adopted for a compact and flexible prototype. The oversize is measured as 46cm*22cm*7cm, i.e., 7 liters. Then the power density is calculated as 2.05kW/L. For comparison, the state-of-art APM usually has a power density <2kW/L[21] [22], for a 3.5kW APM, the overall size is already >7L. No mention within a similar volume, the proposed converter can deliver 3.5kW to LV and 11kW for the HV battery at the same time.

IV. CONCLUSIONS AND FUTURE WORK

This paper proposed a current-fed three-port DCDC converter for the integration of the OBC and APM in EVs. An 11kW+3.5kW prototype is designed. The converter provides multiple functions and presents superiorities over state-of-art approaches in the following aspects: 1) simultaneously charging for HV and LV batteries. 2) full range ZVS operation; 3) near-zero switching-off current for low-side switches; 4) compact and cost-effective output filters design. All these benefits make the proposed converter a good fit for the EV applications saving both cost and space. Future work will include the implementation of the power decoupling and closed-loop control.

Fig. 9 Prototype of 11kW+3.5kW integrated charger with PFC

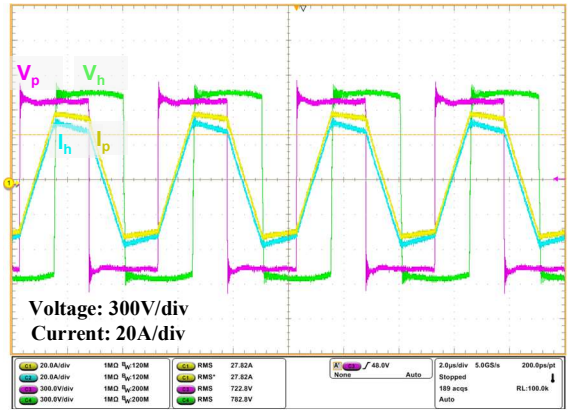

Fig. 10 XFMR voltage/current for HV port (400V/30A output)

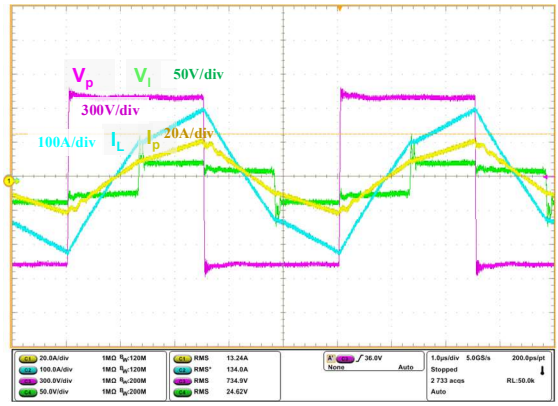

Fig. 11 XFMR voltage/current at LV port (12.3V/250A output)

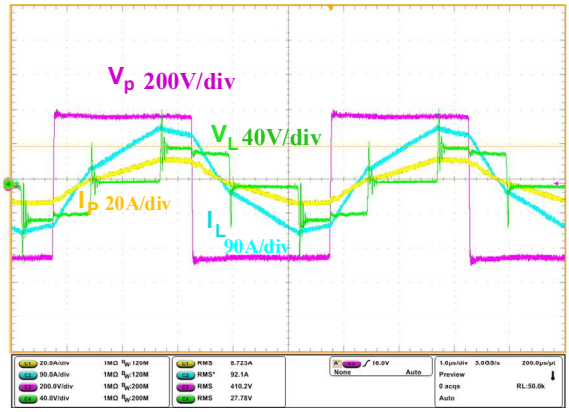

Fig. 12 XFMR voltage/current at LV port (10V/150A output)

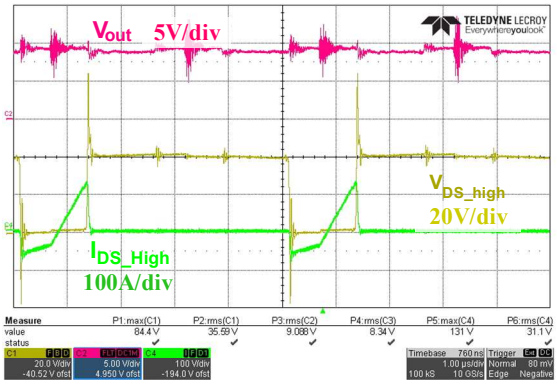

Fig. 13 V_{ds} & I_{ds} of high-side switches at LV port 10V/150A output

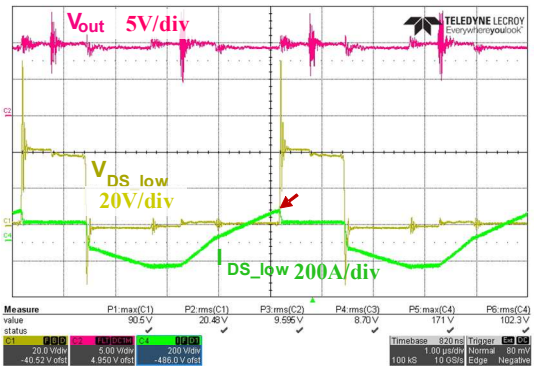

Fig. 14 V_{ds} & I_{ds} of low-side switches at LV port 10V/150A output

REFERENCE

[1] A. Emadi, S. S. Williamson, and A. Khaligh, "Power electronics intensive solutions for advanced electric, hybrid electric, and fuel cell vehicular power systems," *IEEE Transactions on Power Electronics*, vol. 21, no. 3. pp. 567–577, May 2006, doi: 10.1109/TPEL.2006.872378.

[2] J. G. Pinto, V. Monteiro, H. Gonçalves, and J. L. Afonso, "Onboard reconfigurable battery charger for electric vehicles with traction-to-auxiliary mode," *IEEE Trans. Veh. Technol.*, vol. 63, no. 3, pp. 1104–1116, 2014, doi: 10.1109/TVT.2013.2283531.

[3] S. Kim and F. S. Kang, "Multifunctional onboard battery charger for plug-in electric vehicles," *IEEE Trans. Ind. Electron.*, vol. 62, no. 6, pp. 3460–3472, Jun. 2015, doi: 10.1109/TIE.2014.2376878.

[4] V. N. S. R. Jakka, A. Shukla, and G. D. Demetriades, "Dual-Transformer-Based Asymmetrical Triple-Port Active Bridge (DT-ATAB) Isolated DC-DC Converter," *IEEE Trans. Ind. Electron.*, vol. 64, no. 6, pp. 4549–4560, Jun. 2017, doi: 10.1109/TIE.2017.2674586.

[5] Y. K. Tran and D. Dujic, "A multiport isolated DC-DC converter," in *Conference Proceedings - IEEE Applied Power Electronics Conference and Exposition - APEC*, May 2016, vol. 2016-May, pp. 156–162, doi: 10.1109/APEC.2016.7467867.

[6] Y. K. Tran and D. Dujic, "A multiport medium voltage isolated DC-DC converter," in *IECON Proceedings (Industrial Electronics Conference)*, Dec. 2016, pp. 6983–6988, doi: 10.1109/IECON.2016.7793699.

[7] Y. K. Tran, F. D. Freijedo, and D. Dujic, "Multiport energy gateway," *IET Electr. Power Appl.*, vol. 13, no. 10, pp. 1524–1534, Oct. 2019, doi: 10.1049/iet-epa.2018.5907.

[8] X. Gao, H. Wu, Y. Xing, H. Hu, and Y. Zhang, "A new tightly regulated dual output LLC resonant converter with PFM plus secondary side phase-shift control," 2016, doi: 10.1109/ECCE.2016.7854724.

[9] S. Y. Kim, I. Jeong, K. Nam, and H. S. Song, "Three-port full bridge converter application as a combined charger for PHEVs," in *5th IEEE Vehicle Power and Propulsion Conference, VPPC '09*, 2009, pp. 461–465, doi: 10.1109/VPPC.2009.5289810.

[10] H. Ma, Y. Tan, L. Du, X. Han, and J. Ji, "An integrated design of power converters for electric vehicles," in *IEEE International Symposium on Industrial Electronics*, Aug. 2017, pp. 600–605, doi: 10.1109/ISIE.2017.8001314.

[11] G. J. Su and L. Tang, "A new integrated onboard charger and accessory power converter for plug-in electric vehicles," in *2014 IEEE Energy Conversion Congress and Exposition, ECCE 2014*, Nov. 2014, pp. 4790–4796, doi: 10.1109/ECCE.2014.6954057.

[12] D. H. Kim, M. J. Kim, and B. K. Lee, "An integrated battery charger with high power density and efficiency for electric vehicles," *IEEE Trans. Power Electron.*, vol. 32, no. 6, pp. 4553–4565, Jun. 2017, doi: 10.1109/TPEL.2016.2604404.

[13] D. Liu and H. Li, "A ZVS bi-directional DC-DC converter for multiple energy storage elements," *IEEE Trans. Power Electron.*, vol. 21, no. 5, pp. 1513–1517, 2006, doi: 10.1109/TPEL.2006.882450.

[14] H. Tao, A. Kotsopoulos, J. L. Duarte, and M. A. M. Hendrix, "Transformer-coupled multiport ZVS bidirectional DC-DC converter with wide input range," *IEEE Trans. Power Electron.*, vol. 23, no. 2, pp. 771–781, Mar. 2008, doi: 10.1109/TPEL.2007.915129.

[15] C. Zhao, S. D. Round, and J. W. Kolar, "An isolated three-port bidirectional dc-dc converter with decoupled power flow management," *IEEE Trans. Power Electron.*, vol. 23, no. 5, pp. 2443–2453, 2008, doi: 10.1109/TPEL.2008.2002056.

[16] Pit-Leong Wong, Peng Xu, P. Yang, and F. C. Lee, "Performance improvements of interleaving VRMs with coupling inductors," *IEEE Trans. Power Electron.*, vol. 16, no. 4, pp. 499–507, Jul. 2001, doi: 10.1109/63.931059.

[17] Y. Yang, Z. Liu, F. C. Lee, and Q. Li, "Multi-phase coupled and integrated inductors for critical conduction mode totem-pole PFC converter," in *2017 IEEE Applied Power Electronics Conference and Exposition (APEC)*, Mar. 2017, pp. 1804–1809, doi: 10.1109/APEC.2017.7930943.

[18] Z. Guo, K. Sun, T. Wu, and C. Li, "An Improved Modulation Scheme of Current-Fed Bidirectional DC–DC Converters For Loss Reduction," *IEEE Trans. Power Electron.*, vol. 33, no. 5, pp. 4441–4457, May 2018, doi: 10.1109/TPEL.2017.2719722.

[19] Y. Shi, R. Li, Y. Xue, and H. Li, "Optimized Operation of Current-Fed Dual Active Bridge DC-DC Converter for PV Applications," *IEEE Trans. Ind. Electron.*, vol. 62, no. 11, pp. 6986–6995, 2015, doi: 10.1109/TIE.2015.2432093.

[20] X. Sun, X. Wu, Y. Shen, X. Li, and Z. Lu, "A Current-Fed Isolated Bidirectional DC–DC Converter," *IEEE Trans. Power Electron.*, vol. 32, no. 9, pp. 6882–6895, Sep. 2017, doi: 10.1109/TPEL.2016.2623306.

[21] M. R. Ahmed and Y. Li, "A low-cost, high-power-density DC-DC converter for hybrid and electric vehicle applications," Sep. 2019, doi: 10.23919/EPE.2019.8914879.

[22] F. Krismer, J. Biela, and J. W. Kolar, "A comparative evaluation of isolated bi-directional DC/DC converters with wide input and output voltage range," in *Conference Record - IAS Annual Meeting (IEEE Industry Applications Society)*, 2005, vol. 1, pp. 599–606, doi: 10.1109/IAS.2005.1518368.